Optical and Quantum Electronics (2023) 55:1045
https://doi.org/10.1007/s11082-023-05298-3

Design and analysis of quad-band polarization-insensitive infrared perfect metamaterial absorber with a wide-incident angle

Ahmed Elsayed Abouelez[1] · Mohamed Nady Abdulaleem[1]

Received: 21 February 2023 / Accepted: 13 August 2023 / Published online: 21 September 2023

Abstract
There is a pressing demand to design simple absorber structures that support optimal absorption in multi-band to meet different applications. In this work, a novel quad-band infrared perfect metamaterial absorber (QPMA) is proposed and numerically investigated. The structure of the QPMA is composed of coaxial multi-layer dielectric (SiO_2) disks of circular shape with different diameters where each disk is surrounded by a gold ring. All disks are placed on a SiO_2 dielectric spacer and an impermeable gold ground layer. Simulation results reveal that the proposed absorber has four absorption peaks around wavelengths of 1064 nm, 1550 nm, 2080 nm, and 3000 nm. Since these wavelengths correspond to commercially available laser sources, the structure under investigation can be used in different applications such as laser stealth, infrared photodetection, and medical applications. Additionally, the QPMA structure enjoys a good absorption performance for a wide range of incident angles for both TE and TM waves. It achieves absorption greater than 85% at incident angles up to 40° at 1064 nm, and absorption greater than 90% for the other bands at incident angles up to 50°. Moreover, due to the symmetrical shape of the structure, the absorption is insensitive to wave polarization changes.

Keywords Metamaterial · Plasmonic waves · Absorber · Laser stealth · Quad-band absorption

1 Introduction

Metamaterials are artificial materials that are composed of periodic sub-wavelength structures (Pendry 2000; Islam et al. 2016; Wang et al. 2022). Owing to their unique properties, they attracted extensive interest in many applications such as polarization conversion, cloaking, and absorbance (Zhao et al. 2018a, 2018b; Cheng et al. 2019; Xiao et al. 2022). One of the most important applications is the perfect metamaterial absorber (PMA) with near-unity absorption, which is proposed for the first time by Landy et al. (2008) to operate

✉ Ahmed Elsayed Abouelez
a.e.abouelez@eri.sci.eg

[1] Microwave Engineering Department, Electronics Research Institute (ERI), Cairo, Egypt

in the microwave band. Using the appropriate design technique, the intrinsic loss can be controlled, and several types of perfect metamaterial absorbent can be produced at specific wavelengths ranging from the microwave band to the visible and infrared bands (Shen et al. 2011; Bai et al. 2015; Pan et al. 2021; Chai et al. 2022; Khatami et al. 2022). For the infrared and visible bands, the perfect absorption of the PMA is mainly due to the excitation of localized surface plasmon resonance modes at normal/oblique incidents of light waves (Zhang et al. 2011; Liu and Lan 2017; Lei et al. 2018; Cao et al. 2021). When the light waves interact with the metallic nanoparticles, the collective electron oscillations excite the localized surface plasmon resonance (Pu et al. 2011). Based on the requirements of the desired application, the PMA can be classified as PMA with broadband, single-band, and multiband in terms of the bandwidth of the maximum absorption (Liao et al. 2017; Xiong et al. 2020; Dubey et al. 2022). Applications such as energy harvesting and photovoltaic require PMAs with broadband absorption capability (Che et al. 2018; Bendelala et al. 2018; Ehsanikachosang et al. 2022; Lakshmiprabha et al. 2022; Hanif et al. 2023) while sensing and photo-detection applications require PMAs with ultra-narrow single or multi-band absorption capability (Shi et al. 2020; Korkmaz et al. 2022; Liao et al. 2022; Yi et al. 2022). The typical metamaterial absorber is a three-part structure called metal-dielectric-metal (MDM); a dielectric substrate part sandwiched between the bottom part which is bulk metal acts as a back reflector and a top geometrical metal pattern part. In addition, many other PMAs are based on dielectric-dielectric-metal (Liao et al. 2017) or all-metal structures (Zhao et al. 2018b; Zhang et al. 2021).

In the quest for visible and infrared multi-band PMA absorbers, several designs have been investigated numerically or experimentally. Bai et al. (2015) proposed a polarization-insensitive dual-band infrared PMA with a wide-incident-angle. The PMA was made of double L-shaped gold pieces on a SiC dielectric spacer and gold ground layer. In (Liao et al. 2022), a dual-band guided-laser absorber at wavelengths of 1064 nm and 1550 nm was investigated. This absorber consists of periodic silicon squares on a silicon film and a nickel layer (i.e., dielectric-dielectric-metal structure). In (Shi et al. 2020), a PMA was proposed to make ultra-narrow triple absorption bands in the near-infrared for sensing applications. This PMA is composed of a periodic arrangement of metallic nanodisks etched with regular prismatic holes on the dielectric-metal bi-layer films. Based on a periodic array of silicon nanorod resonator and metal substrate, a quad-band perfect absorber for visible light is investigated by Cao and Cheng (2018). In this design, the proposed absorber achieved absorbance greater than 90% at wavelengths around 0.69 μm, 0.657 μm, 0.622 μm, and 0.594 μm. Zhang et al. (2021) introduced a quad-band perfect absorber that is based on an all-metal nanostructure metasurface for refractive index applications in the infrared band. Based on numerical analysis, the proposed absorber achieved absorbance greater than 99% at wavelengths around 3.48 μm, 1.25 μm, 1 μm, and 0.87 μm. In (Korkmaz et al. 2022), the authors presented an experimental study on quad-band PMA for biosensing applications. The design is based on an MDM structure where MgF_2 dielectric spacer was inserted between an optically thick gold layer and a patterned gold shape. The four peak absorption of the proposed design covers a spectral range from 1.8 μm to 10 μm.

In this work, we introduce a novel design of a quad-band infrared perfect metamaterial absorber (QPMA). The proposed absorber achieves quad-band perfect absorption around specific wavelengths. These wavelengths are tuned to be corresponding to Nd: YAG laser (1064 nm), the most important laser wavelength in communication systems (1550 nm), Ho: YAG laser (2080 nm), and mid-infrared laser for medical applications (3000 nm) which is close to Er: YAG laser wavelength (i.e., 2940 nm). Nd: YAG laser is used in laser radar systems and free space laser communications, 1550 nm laser is used in most optical

communication systems (optical fiber or free-space optics communications), Ho: YAG laser and Er: YAG lasers are used basically in medical applications. Thus, it is expected that the proposed absorber structure may be useful for different practical applications such as laser stealth (Liao et al. 2022), photodetection (Yu et al. 2016; Song et al. 2018; Xie et al. 2022), and medical applications (Wu et al. 2016).

The design is based on an improved MDM structure where its top pattern consists of coaxial multi-layer dielectric (SiO_2) disks of circular shape with different diameters. Each disc is surrounded by a gold (Au) metal ring. Each Au ring is responsible, effectively, for one resonance wavelength and is optimized with its neighbor to achieve perfect absorption at the desired wavelength. Each resonance of the QPMA structure is a good consequence of the related geometrical parameters (mainly the radius and height of the Au ring), therefore, good tunability for each resonant wavelength can be achieved. Owing to the simplicity and symmetry of the proposed structure, it enjoys several benefits, such as polarization insensitivity and coverage of wide-incident angles.

The rest of the paper is organized as follows. Section 2 introduces the proposed structure in which the shape, dimensions, and materials are explained. The effects of the variations in incident, polarization, and structure bending angles on the performance of the proposed absorber are studied in Sect. 3. A comparison to the recently proposed multi-band absorbers is dedicated in Sect. 4. Finally, we conclude the obtained results in Sect. 5.

2 Structure design

The proposed QPMA structure consists of periodic cells. The schematic of the unit cell structure is illustrated in Fig. 1a, b; each unit cell is composed of a coaxial multilayer of SiO2 dielectric disks each disk surrounded by an Au metal ring. The dielectric disks are labeled, from bottom to top, by D1, D2, D3, and D4. On the other hand, the metal rings are labeled, from bottom to top, by M1, M2, M3, and M4. The structure is built on a substrate of SiO2. This substrate is built over a continuous layer of Au which acts as a back reflector. The unit cell period along the x and y directions equals $\boldsymbol{P}$. The Au back reflector has a thickness $\boldsymbol{Tm}$ while the SiO2 substrate layer has a thickness $\boldsymbol{Td}$. The radii of the four gold rings from bottom to top are $\boldsymbol{Rg}1$, $\boldsymbol{Rg}2$, $\boldsymbol{Rg}3$, and $\boldsymbol{Rg}4$, respectively, while their thicknesses are labeled $\boldsymbol{Tr}1$, $\boldsymbol{Tr}2$, $\boldsymbol{Tr}3$, and $\boldsymbol{Tr}4$. The golden rings have widths of $\boldsymbol{Wg}1$, $\boldsymbol{Wg}2$, $\boldsymbol{Wg}3$, and $\boldsymbol{Wg}4$. The proposed structure ends with a golden disk with a diameter $\boldsymbol{D}$ and thickness $\boldsymbol{Tr}5$.

We numerically study the electromagnetic behavior of the proposed QPMA by frequency domain solver in the commercial CST Microwave Studio which is based on the finite element method. The complex refractive index data of Au metal is obtained from (Ciesielski et al. 2018). Furthermore, the refractive index of the SiO_2 dielectric layers is assumed to be 1.45.

The optimized parameters of the proposed structure used in the simulation are as follows (units in nm): $\boldsymbol{P} = 634$, $\boldsymbol{Tm} = 100$, $\boldsymbol{Td} = 50$, $\boldsymbol{Tr}1 = 65$, $\boldsymbol{Tr}2 = 65$, $\boldsymbol{Tr}3 = 41$, $\boldsymbol{Tr}4 = 22$, $\boldsymbol{Tr}5 = 30$, $\boldsymbol{Rg}1 = 264$, $\boldsymbol{Wg}1 = 61$, $\boldsymbol{Rg}2 = 163$, $\boldsymbol{Wg}2 = 25$, $\boldsymbol{Rg}3 = 101$, $\boldsymbol{Wg}3 = 20$, $\boldsymbol{Rg}4 = 62$, $\boldsymbol{Wg}4 = 24$, $\boldsymbol{D} = 76$.

Due to the periodicity of the structure, we simulate only one unit cell. Therefore, the boundary conditions in the x and y directions are set as a unit cell while the perfectly matched layer boundary condition is used in the positive z-direction.

The structure under investigation has a symmetrical behavior in the x and y-directions. As indicated in Fig. 1c, the transverse electric (TE) or transverse magnetic (TM) incident

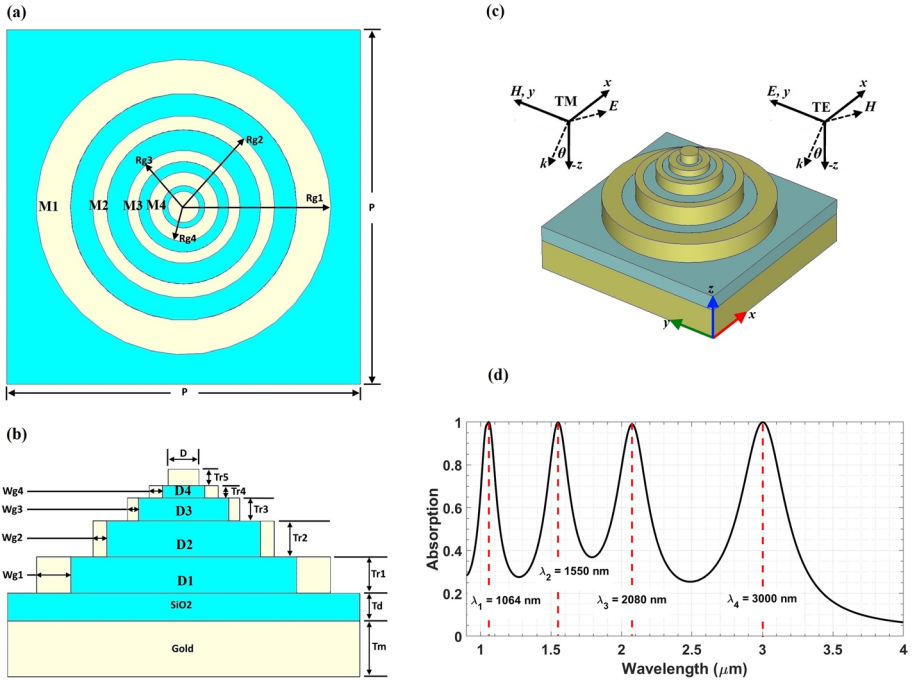

Fig. 1 Geometrical model of the proposed QPMA. **a** Top view. **b** Side view. **c** 3D view. **d** The absorption spectra of the QPMA under normal incidence

waves are propagated in the negative z-direction. The TE/TM wave is incident on the structure in the x–z incidence plane with an incident angle θ relative to the negative z-direction. The spectral absorptivity $\boldsymbol{A}(\boldsymbol{\omega})$ can be calculated by $\boldsymbol{A}(\boldsymbol{\omega}) = 1 - \boldsymbol{R}(\boldsymbol{\omega}) - \boldsymbol{T}(\boldsymbol{\omega})$, where $\boldsymbol{R}(\boldsymbol{\omega}) = |\boldsymbol{S}_{11}|^2$ and $\boldsymbol{T}(\boldsymbol{\omega}) = |\boldsymbol{S}_{21}|^2$ are the spectral reflection and transmission, respectively. $\boldsymbol{S}_{11}$ and $\boldsymbol{S}_{21}$ denotes the S-parameters. Since the thickness of the Au back reflector is much larger than its skin depth in the infrared, the spectral transmission can be neglected, i.e. $\boldsymbol{T}(\boldsymbol{\omega}) = 0$.

3 Results and discussions

Figure 1d displays the absorption spectra in the band from 0.9 to 4 μm for normal incidence of TE or TM electromagnetic waves. It can be noted that under the optimized structure parameters, which were introduced in the previous section, we obtained four maximum absorption peaks around the wavelengths of 1064 nm, 1550 nm, 2080 nm, and 3000 nm with absorption values of 99.9%, 99.9%, 99.1%, and 99.9%, respectively. These values of absorptivity indicate perfect absorption at the four wavelengths.

To explain the nature of these four absorption peaks, absorption spectra are simulated for the sequential steps of construction growth direction (i.e., the effect of adding a layer of SiO_2 surrounded by an Au ring to the structure). This process is depicted in Fig. 2. Figure 2a introduces the absorption spectra for the first layer, which has a radius of $Rg1$. It can be noted that the structure with this ring has a single absorption peak at a wavelength

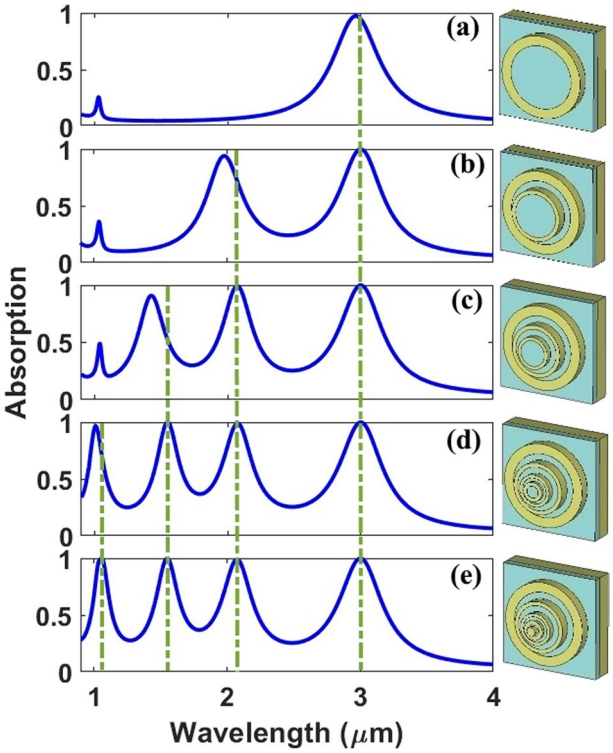

Fig. 2 Absorption spectra for different stages of the design, **a** one ring, **b** two rings, **c** three rings, **d** four rings, and **e** full QPMA structure

of 2965.5 nm with an absorptivity of 97.3%. As shown in Fig. 2b, after adding the second layer, which has a radius of $Rg2$, another absorption peak appears at a wavelength of 1982 nm with an absorptivity of 94%. Also, it can be noted that the addition of the second layer causes a red shift to the first peak from 2965.5 to 3000 nm and enhance the value of its absorption to be equal to 99.9%. Figure 2c illustrates the effect of adding the third layer, which has a radius of $Rg2$, on the absorption spectra. Another absorption peak appears at a wavelength of 1428 nm with an absorptivity of 90.85%. Also, the addition of the third layer leads to a red shift to the second peak to a wavelength around 2080 nm with enhanced absorptivity to become 99.1% while it does not affect the first peak. Figure 2d shows the effect of adding the fourth layer to the structure. This addition results in the appearance of the fourth peak at the wavelength of 1010 nm with an absorptivity of 96.5% and a red shift to the third peak to a wavelength around 1550 nm with an absorptivity of 99.9% while it does not affect the first and second peaks. Finally, to adjust the fourth peak to be at a wavelength of 1064 nm with absorptivity of 99.9%, a golden disk of radius $Rg5$ is added on the top of the fourth layer as shown in Fig. 2e. From the description of Fig. 2, we can conclude that adding a new layer adds a new resonance and adjusts the previous resonance to a desired wavelength with perfect absorbability.

The metamaterial properties and the concept of impedance matching are discussed in the following subsections. The electric and magnetic field distributions at each resonance wavelength are also displayed and discussed. The effects of the variation in polarization and incident angles on the performance of the proposed QPMA structure are studied. Finally, the bending effect on the proposed QPMA structure is investigated.

3.1 Metamaterial properties and impedance matching

In metamaterial absorption, impedance matching is the keystone in the absorption operation. The effective medium theory states that the metamaterial equivalent permittivity, ε_{eq}, and equivalent permeability, μ_{eq}, depending on the effective medium weight of each layer of the structure which can be calculated by Eqs. (1) and (2), respectively (Sun et al 2022)

$$\varepsilon_{eq} = \varepsilon_m V_m + \varepsilon_d V_d + \varepsilon_0 \left(1 - V_m - V_d\right) \tag{1}$$

$$\mu_{eq} = \mu_m V_m + \mu_d V_d + \mu_0 \left(1 - V_m - V_d\right) \tag{2}$$

whereV_m, V_d, and $\left(1 - V_m - V_d\right)$ are the volume fraction of Au, SiO_2, and air w.r.t. total volume in each layer, respectively. ε_m and μ_m symbolize the permittivity and the permeability of Au while ε_d and μ_d denote the permittivity and the permeability of SiO2. ε_0 and μ_0 is the permittivity and permeability of the air. Based on electromagnetic theory, the equivalent relative impedance of each layer is $Z_i = \sqrt{\mu_{eq}/\varepsilon_{eq}}/Z_0$ where $Z_0 = 120\pi\ \Omega$ is the free space characteristic impedance. Then, the total relative impedance can be approximated as the series equivalent of these layers' relative impedances ($Z(\omega) \approx \sum_i Z_i$). This relative impedance can be calculated in terms of S-parameters as

$$Z(\omega) = \sqrt{\frac{\left(1 + S_{11}\right)^2 - S_{21}^2}{\left(1 - S_{11}\right)^2 - S_{21}^2}} \tag{3}$$

We show in Fig. 3 the real and imaginary components of the relative input impedance given by Eq. (3). It is clear from this figure, that the real component of the relative impedance at the four resonances is approximately equal to one (i.e., Re (z) ≈1), while the imaginary component is near zero (i.e., Im (z) ≈0). These results indicate that the impedance of the QPMA is in a good matching with the free space characteristic impedance at the four resonance wavelengths, hence, no reflection occurs and perfect absorption is achieved.

3.2 Electric and magnetic field distributions

To investigate the concept of absorption of QPMA, we introduce the absolute value of the electric field, $|E|$, and the magnetic field, $|H|$, distributions of the absorber, at (a) λ_1

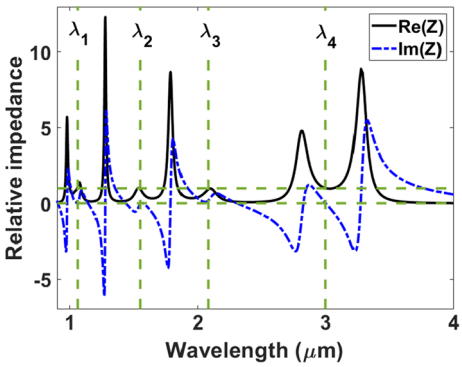

Fig. 3 The real and imaginary components of the relative impedance of the proposed QPMA

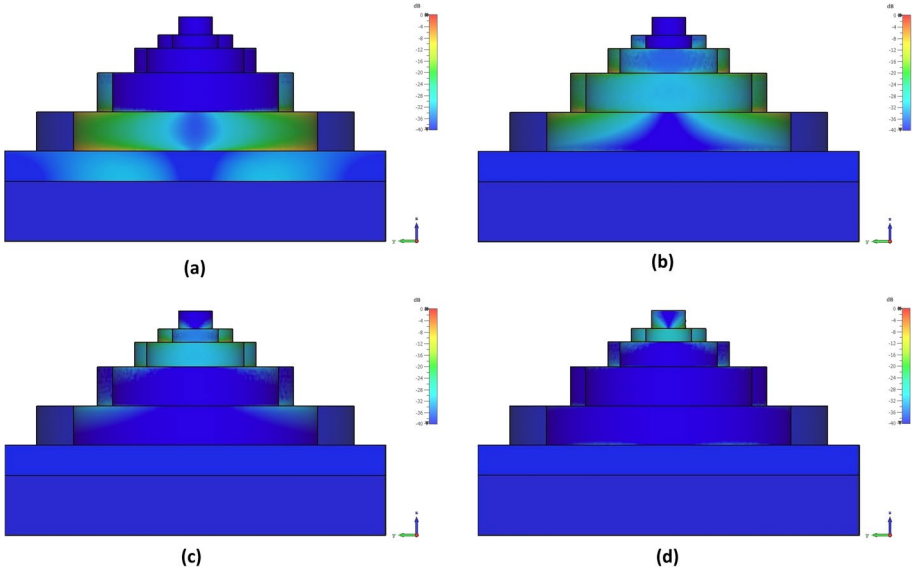

Fig. 4 y–z cross-section view for $|E|$ field distribution at **a** λ_1=3000 nm, **b** λ_2=2080 nm, **c** λ_3=1550 nm, and **d** λ_4=1064 nm

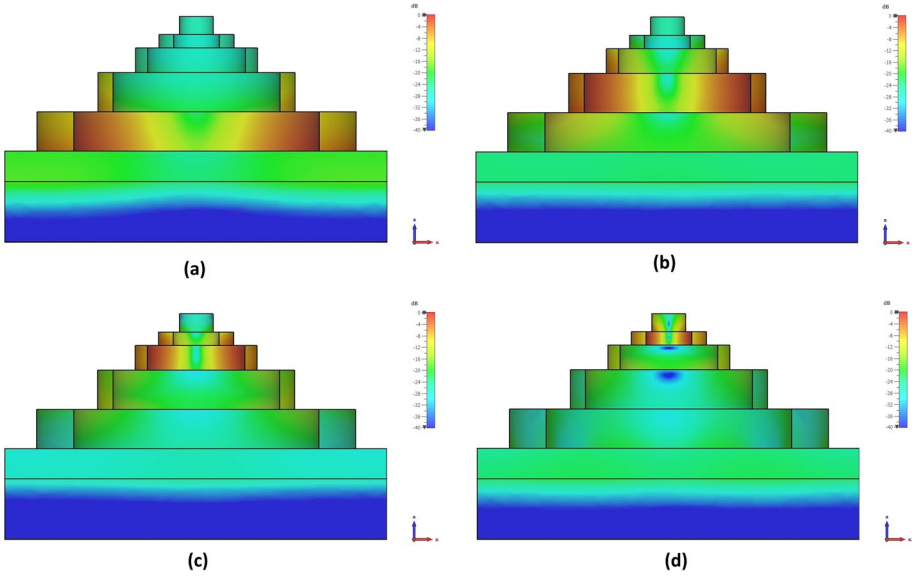

Fig. 5 x–z cross-section view for $|H|$ field distribution at **a** λ_1=3000 nm, **b** λ_2=2080 nm, **c** λ_3=1550 nm, and **d** λ_4=1064 nm

=3000 nm, (b) λ_2=2080 nm, (c) λ_3=1550 nm, and (d) λ_4=1064 nm, in Figs. 4 and 5, respectively. Figures 4 shows the y–z plane cross-section view for $|E|$ field distribution while Fig. 5 shows x–z plane cross-section view for $|H|$ field distribution. It is clear from

Figs. 4a and 5a, corresponding to the wavelength of 3000 nm, that $|E|$ field and $|H|$ field distributions are mainly concentrated inside the first dielectric disk, D1, between the rings M1 and M2, with some little distribution inside the substrate. The concentration of the electric field between these rings, M1 and M2, indicates an equivalent capacitance while the magnetic field concentration indicates an inductance behavior of this region. The interaction between the capacitance and inductance leads to resonance at the first band i.e., 3000 nm. This behavior confirms the result shown in Fig. 2b in which the resonance at 3000 nm comes mainly due to the ring M1 with fine tuning from ring M2. Similarly, at a wavelength of 2080 nm, it can be noted from Figs. 4b and 5b that $|E|$ field and $|H|$ field distributions are mainly concentrated at the dielectric D2 between the ring M2 and M3, which results in a peak absorption at that frequency. Also, the same behavior takes place between rings M3 and M4 at the wavelength of 1550 nm as indicated in Figs. 4c and 5c. Finally, for the peak absorption at a wavelength of 1064 nm, Figs. 4d and 5d show that the $|E|$ field and $|H|$ field distributions are mainly concentrated inside the top dielectric disk, D4, between the ring M4 and the top metal disk.

3.3 Effect of polarization angle variation

The polarization insensitivity of the proposed QPMA is studied in this subsection. The electromagnetic wave is incident vertically on the proposed absorber surface. The polarization angle,φ, is defined as the angle between the electric field and the x-axis. This definition is illustrated in Fig. 6a. The effect of varying the polarization angle of the incident wave on the absorption of the proposed absorber is presented in Fig. 6. The obtained results reveal that when the polarization angle varies, the peaks of the absorption for the quad bands remain unchanged. Thus, the proposed QPMA is insensitive to the variation of the polarization angle.

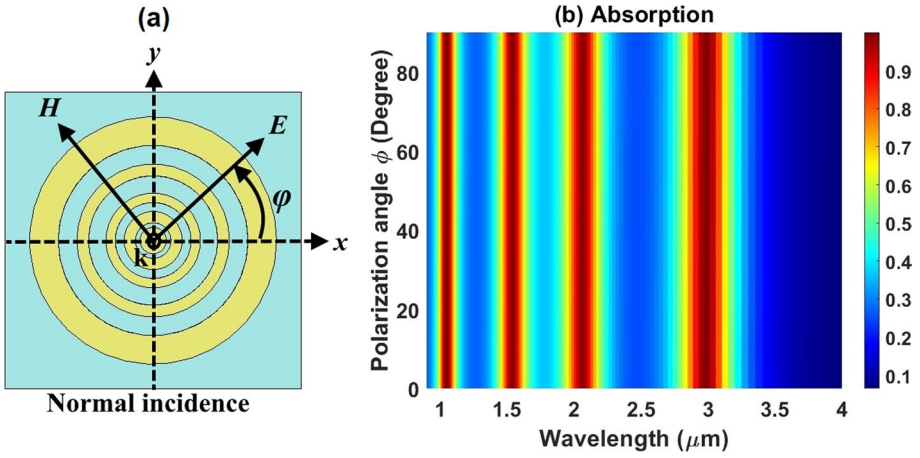

Fig. 6 **a** Polarization angle definition (normal incidence). **b** Absorption spectra versus the polarization angle at $\theta = 0°$

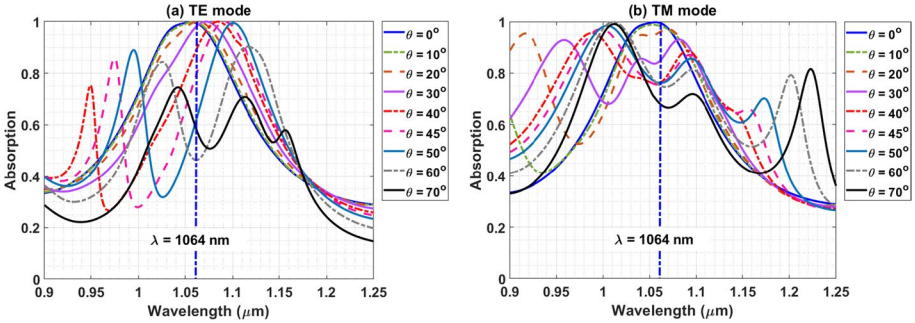

Fig. 7 Absorption spectra of the proposed QPMA for different incident angles at 1064 nm band for **a** TE mode and **b** TM mode

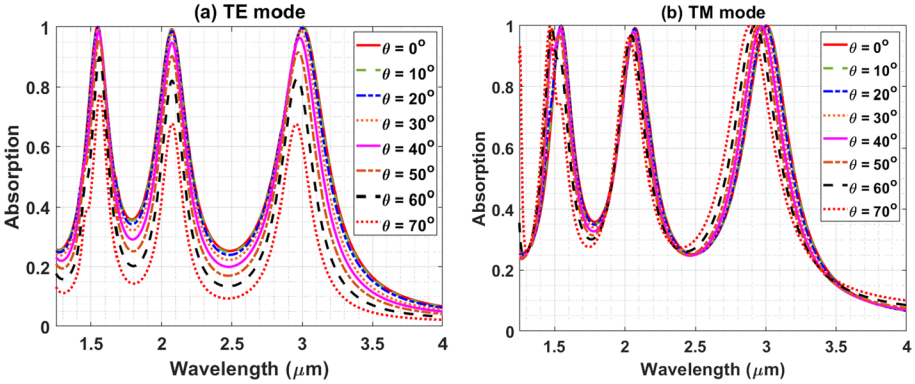

Fig. 8 Absorption spectra of the proposed QPMA for different incident angles at 1550 nm, 2080nm, and 3000 nm bands for **a** TE mode and **b** TM mode

3.4 Effect of incident angle variation

In practical applications, the effect of large-angle absorption plays a significant role in designating the performance of the absorber. In this subsection, we address the effect of incident angle for both TE and TM modes. Owing to the high sensitivity of the proposed absorber at 1064 nm wavelength to the variation of incident angle, as observed from simulation results, the results of this effect for TE and TM modes are introduced in Fig. 7a, b for 1064 nm wavelength, only, while Fig. 8a, b present the counterpart results for the remaining triple bands.

At $\theta = 0$ (i.e., normal incidence), due to the symmetrical geometry of the proposed absorber, it can be noted that for both TE and TM, the proposed absorber can trap the incident infrared waves regardless of their polarization.

For the 1064 nm wavelength, Fig. 7a shows the absorption spectra in the band from 0.9 to 1.25 μm for TE mode. As can be observed, as the incident angle increases the peak absorption around 1064 nm tends to make a red shift up to 1100 nm at $\theta = 50°$ then the absorption peak drops below 90% at a wavelength of 1120 nm and incident angle of $\theta = 60°$. Also, other absorption peaks are observed at incident angles greater than $\theta = 30°$. These peaks, also, tend to make red shift with the increase of incident angle. The proposed

structure can perform an absorption peak of 90% around 1064 nm at an incident angle of $\theta = 40°$ at TE mode. On the other hand, as indicated in Fig. 7b for the TM mode, peak absorption around 1064 nm tends to make a red shift with a continuously decreasing in its value. In addition, other absorption peaks can be observed at incident angles greater than $\theta = 10°$ which, also, tend to make red shift with the increase of incident angle. The proposed structure can perform an absorption peak of 85% around 1064 nm at an incident angle of $\theta = 30°$ at TM mode.

Furthermore, we investigate the absorber performances for the triple bands, 1550 nm, 2080 nm, and 3000 nm under several incident angles from 0° to 70° for both TE and TM modes are illustrated in Fig. 8a, b, respectively. As shown in Fig. 8a, in the case of TE mode, it can be noted that as the incident angle increases the absorption peak values decrease for all bands. Also, with the increase of incident angle value, the absorption peaks around the 3000 nm band tend to make a blue shift while the absorption peaks around the 1550 nm band tend to make a red shift. The proposed absorber can perform absorption greater than 90% for all three bands under consideration at incident angles up to 50°. For incident angles larger than 50°, the absorption intensity of the triple-band peaks degrades rapidly. This is because the magnetic field component in the x–y plane is $H_{x-y} = Hcos\theta$ which is required to excite the magnetic polaritons (Bai et al. 2015; Ye et al. 2010), where H is the incident magnetic field intensity. Because the intensity drops rapidly at $\theta > 50°$, the magnetic resonance becomes weaker, hence, we observed lower absorption. On the other hand, in the case of TM mode, shown in Fig. 8b, the triple absorption peaks intensity remains above 99%. This is due to the stability in the magnetic incident field component in the direction of magnetic polaritons oscillations. Also, it can be noted the absorption peaks around the center wavelengths of the triple bands tend to make, only, a blue shift with an insignificant decrease in its peak value. Yet, due to the blue shift from the center wavelengths, there is a reduction in the absorption values at the center wavelengths of the triple bands. The proposed absorber can perform absorption greater than 90% at the center wavelength of all three bands under consideration at incident angles up to 50°. The slight blue shift of the three absorption peaks arises, mainly, due to the off-phase oscillating effect (Ye et al. 2010).

3.5 Effect of structure bending

In some applications, absorbers can be mounted on a curved structure or suffer from mechanical deformations (Deng et al. 2018; Ordek et al. 2022), therefore, this sub-section is devoted to examining the bending effect on our proposed QPMA. The periodic structure is bent to be cylindrical where the cylinder axis lies in the y direction. The whole structure may be bent with a negative angle (i.e., convex bending) or with a positive angle (i.e., concave bending). These behaviors are illustrated in Fig. 9a, b, respectively. In CST, the cylindrical bending tool is used to bend the structure with a bending angle (BA) from 10^o to -10^o. Under normal incidence, the absorption spectra for both TE and TM are presented at different BAs as shown in Fig. 9c, d, respectively. For TE mode, it can be noted that the concave bending causes a blue shift for all four resonances while the convex bending causes a red shift. These shifts in resonance wavelengths are.

more significant on longer resonance wavelengths (i.e., 2080 and 3000 nm) and become less significant at shorter wavelengths (i.e., 1550 nm and 1064 nm). This is due to the rings with large radii being affected by bending more significantly than the rings with smaller radii. For TM mode, these mentioned effects (i.e., blue shift for concave bending and red

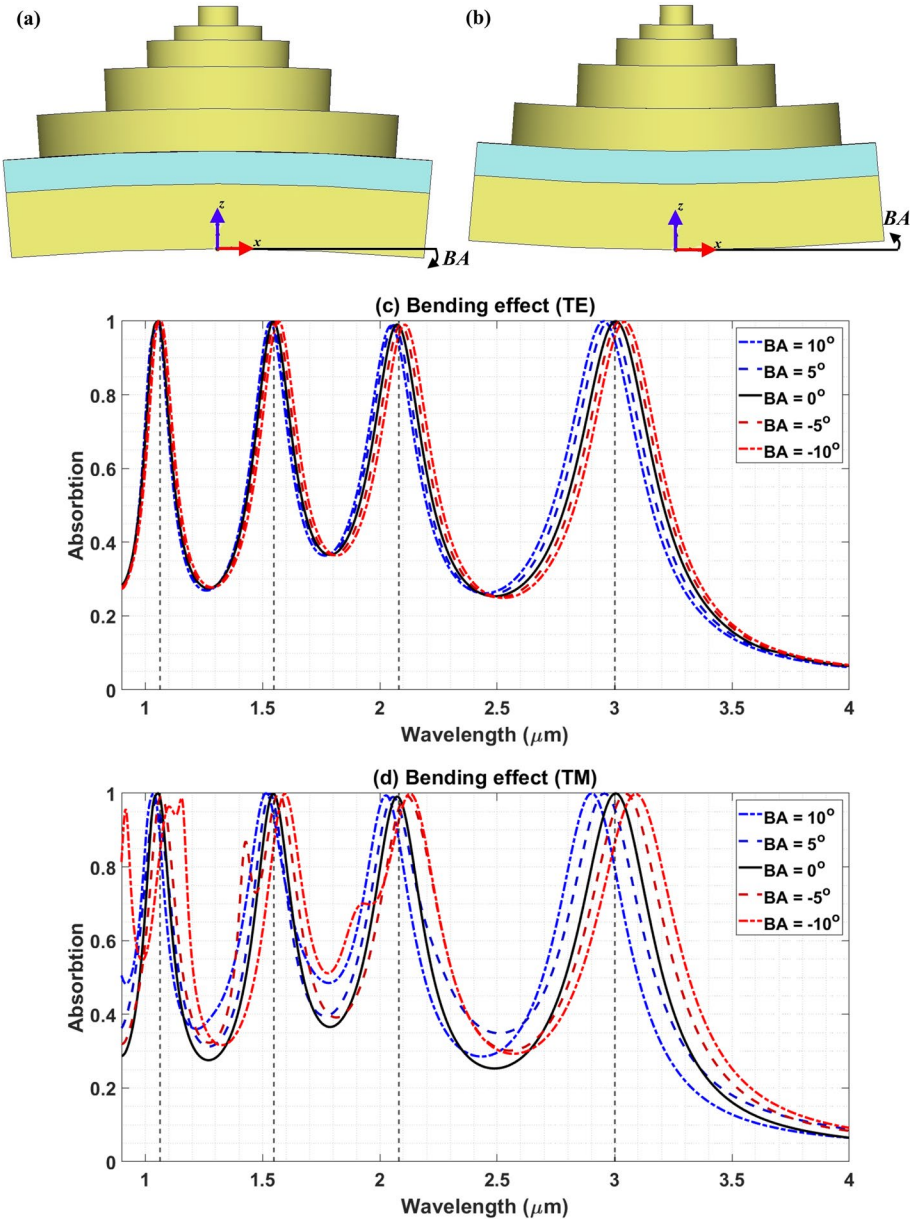

Fig. 9 Structure bending effect. **a** Convex (negative angle) bent shape **b** concave (positive angle) bent shape, Absorption spectra of the proposed QPMA under different bending angles for **c** TE mode and **d** TM mode

Table 1 Comparison between the proposed QPMA and recently reported multi-band absorbers

Reference	No. of Peaks	Wavelengths	Materials	Average absorption (normal incidence)	Laser sources compatibility	Methods of verification	absorption at a wide-incident angle	Polarization sensitivity
Liao et al. 2022	2	1550 nm and 1064 nm	Si- Ni	> 94.4%	yes	simulation	yes	Insensitive
Yi et al. 2022	3	908 nm, 1085 nm, and 1216 nm	Ag-Dielectric-Ag	99.5%	yes	simulation	yes	Insensitive
Cao & Cheng 2018	4	690 nm, 657 nm, 622 nm, and 594 nm	Si-Au	> 92.2%	N/A	simulation	N/A	Insensitive
Zhang et al. (2021)	4	3480 nm, 1250 nm, 1000 m, and 870 nm	Au	> 99%	N/A	simulation	N/A	N/A
Korkmaz et al. 2022	4	In the range from 1.8 to 10 μm)	MgF_2/Au	25% (first peak), (85% for remaining peaks)	N/A	Experimental and simulation	N/A	N/A
This work	4	1064 nm, 1550 nm, 2080 nm, and 3000 nm	Au/SiO_2	> 99%	yes	simulation	yes	Insensitive

shift for convex bending in resonance wavelengths) are larger than its counterpart in the TE mode.

4 Comparison study

In this section, the performance of our proposed QPMA is compared to the recently published works in visible and infrared multi-band absorbers. The comparison is based on, namely, the number of bands, materials type, methods of verification, compatibility with commercially available laser sources, wide-incident angle capability, and polarization sensitivity as introduced in Table 1. Compared to the recently proposed multi-band absorbers, our proposed absorber in this work shows compatibility with four commercially available laser sources with near-unity absorption and the capability of good absorption at a wide-incident angle and insensitive to the variations in the polarization angle.

5 Conclusion

This paper presents a numerical demonstration of the absorption performance of the QPMA in the infrared band. The structure of the absorber is composed of coaxial multi-layer SiO_2 disks of circular shape with different diameters. Each disk is surrounded by a gold ring and all coaxial disks are placed on a SiO_2 dielectric spacer and a thick gold ground layer. At the normal incident, the absorption of the quad-band is greater than 99% at wavelengths of 1064 nm, 1550 nm, 2080 nm, and 3000 nm. Also, the effect of the incident angle variations on the stability of the perfect absorber is examined for both TE and TM. The simulation results show that the QPMA has good performance for both TE and TM modes over a wide range of incident angles. It was observed that the absorption is greater than 85% at incident angles up to 40° at 1064 nm, and absorption was greater than 90% for the other bands at incident angles up to 50°. Additionally, the bending effects on the proposed absorber are addressed. The results reveal that the concave and convex bends cause blue shifts and red shifts in the resonance wavelength. Generally, due to the symmetry of the proposed shape, the absorber enjoys the polarization-insensitive property. This quad-band polarization-independent and wide-angle infrared absorber can be used in many applications such as laser stealth, infrared photodetection, and medical applications.

Acknowledgements The authors would like to thank Prof. Essam A. Eldiwany at Electronics Research Institute for his insightful discussions.

Author contribution All authors contributed equally to the study's conception and design. Analysis, simulations, and verifications were performed by A.E.A. and M.N.A. The first draft of the manuscript was written by A.E.A. and M.N.A. All authors read and approved the final manuscript.

Funding Open access funding provided by The Science, Technology & Innovation Funding Authority (STDF) in cooperation with The Egyptian Knowledge Bank (EKB). Funding is not applicable to this article (no funds for this research).

Data availability Data sharing is not applicable to this article as no datasets were generated or analyzed during the current study. The availability of data and material is not applicable as there are no data sets used.

Declarations

Competing interests The authors declare no competing interests.

Conflict of interest We declare that the authors have no competing interests.

Ethical approval Fortunately, there are no ethical concerns associated with this work.

References

Bai, Y., Zhao, L., Ju, D., Jiang, Y., Liu, L.: Wide-angle, polarization-independent and dual-band infrared perfect absorber based on L-shaped metamaterial. Opt. Express **23**(7), 8670–8680 (2015)

Bendelala, F., Cheknane, A., Hilal, H.S.: A broad-band polarization-insensitive absorber with a wide angle range metamaterial for thermo-photovoltaic conversion. Opt. Quant. Electron. **50**, 1–10 (2018)

Cao, C., Cheng, Y.: Quad-band plasmonic perfect absorber for visible light with a patchwork of silicon nanorod resonators. Materials **11**(10), 1954 (2018)

Cao, S., Jin, Y., Dong, H., Guo, T., Liu, Z., He, J., He, S.: High-temperature ultra-broad UV–MIR high-efficiency absorber based on double ring-shaped titanium nitride resonators. Opt. Commun. **485**, 126730 (2021)

Chai, M., Wang, Y., Chen, C., Zhao, Z., Jin, M., He, T.: Metamaterials-based photoelectric conversion: from microwave to optical range. Laser Photonics Rev. **16**(3), 2100458 (2022)

Che, Z., Tian, C., Chen, X., Wang, B., Wang, K.: Design of a broadband infrared metamaterial absorber. Optik **170**, 535–539 (2018)

Cheng, Y., Fan, J., Luo, H., Chen, F.: Dual-band and high-efficiency circular polarization convertor based on anisotropic metamaterial. IEEE Access **8**, 7615–7621 (2019)

Ciesielski, A., Skowronski, L., Trzcinski, M., Górecka, E., Trautman, P., Szoplik, T.: Evidence of germanium segregation in gold thin films. Surf. Sci. **674**, 73–78 (2018)

Deng, B., Xu, R., Zhao, K., Lu, Y., Ganguli, S., Cheng, G.J.: Composite bending-dominated hollow nanolattices: A stiff, cyclable mechanical metamaterial. Mater. Today **21**(5), 467–474 (2018)

Dubey, S.K., Kumar, A., Dayal, G., Pathak, A., Srivastava, S.K.: Polarization insensitive metamaterial based electromagnetic multiband absorber in the long-wave infrared (LWIR) region. Opt. Laser Technol. **156**, 108511 (2022)

Ehsanikachosang, M., Karimi, K., Rezaei, M.H., Pourmajd, H.: Metamaterial solar absorber based on titanium resonators for operation in the ultraviolet to near-infrared region. JOSA B **39**(12), 3178–3186 (2022)

Hanif, A., Hakim, M.L., Alam, T., Islam, M.T., Alsaif, H., Soliman, M.S.: Polarization insensitive oblique incident angle stable ultra-thin nano ring resonator-based metamaterial absorber for visible and near-infrared region applications. Opt. Laser Technol. **164**, 109494 (2023)

Islam, S.S., Faruque, M.R.I., Islam, M.T.: An object-independent ENZ metamaterial-based wideband electromagnetic cloak. Sci. Rep. **6**(1), 1–10 (2016)

Khatami, S.A., Rezaei, P., Zamzam, P.: Quad band metal-dielectric-metal perfect absorber to selective sensing application. Opt. Quant. Electron. **54**(10), 1–14 (2022)

Korkmaz, S., Oktem, E., Yazdaanpanah, R., Aksu, S., Turkmen, M.: Experimental study of a quad-band metamaterial-based plasmonic perfect absorber as a biosensor. Molecules **27**(14), 4576 (2022)

Lakshmiprabha, K.E., Govindaraju, C., Mahendran, G.: Broadband plus-shaped metasurface absorber based on graphene for visible and ultraviolet regions. Opt. Quant. Electron. **54**(12), 1–12 (2022)

Landy, N.I., Sajuyigbe, S., Mock, J.J., Smith, D.R., Padilla, W.J.: Perfect metamaterial absorber. Phys. Rev. Lett. **100**(20), 207402 (2008)
Lei, L., Li, S., Huang, H., Tao, K., Xu, P.: Ultra-broadband absorber from visible to near-infrared using plasmonic metamaterial. Opt. Express **26**(5), 5686–5693 (2018)
Liao, X., Zeng, J., Zhang, Y., Zhao, J., He, X. and Yang, J.: A dual-band guided-laser absorber based on silicon-nickel metasurface. In Photonics, 9(10), 682 (2022)
Liao, Y.L., Zhao, Y.: An ultra-narrowband absorber with a dielectric-dielectric-metal structure based on guide-mode resonance. Opt. Commun. **382**, 307–310 (2017)
Liu, P., Lan, T.: Wide-angle, polarization-insensitive, and broadband metamaterial absorber based on multi-layered metal–dielectric structures. Appl. Opt. **56**(14), 4201–4205 (2017)
Ordek, B., Esat, V., Sabah, C.: Effects of bending on the electro-optical properties of a wide-band silicon-carbon nanotube-based metamaterial absorber. Mater. Today Commun. **32**, 104073 (2022)
Pan, H., Zhang, H., Tian, X., Zhang, D.: Broadband terahertz absorber with gradient ring resonators based on a discrete spiral topological distribution. JOSA B **38**(3), 850–857 (2021)
Pendry, J.B.: Negative refraction makes a perfect lens. Phys. Rev. Lett. **85**(18), 3966 (2000)
Pu, M., Hu, C., Wang, M., Huang, C., Zhao, Z., Wang, C., Feng, Q., Luo, X.: Design principles for infrared wide-angle perfect absorber based on plasmonic structure. Opt. Express **19**(18), 17413–17420 (2011)
Shen, X., Cui, T.J., Zhao, J., Ma, H.F., Jiang, W.X., Li, H.: Polarization-independent wide-angle triple-band metamaterial absorber. Opt. Express **19**(10), 9401–9407 (2011)
Shi, L., Shang, J., Liu, Z., Li, Y., Fu, G., Liu, X., Pan, P., Luo, H., Liu, G.: Ultra-narrow multi-band polarization-insensitive plasmonic perfect absorber for sensing. Nanotechnology **31**(46), 465501 (2020)
Song, S., Ma, X., Pu, M., Li, X., Guo, Y., Gao, P., Luo, X.: Tailoring active color rendering and multiband photodetection in a vanadium-dioxide-based metamaterial absorber. Photonics Res. **6**(6), 492–497 (2018)
Sun, X., Li, Y., Huang, Y., Cheng, Y., Wang, S., Yin, W.: Achieving super broadband electromagnetic absorption by optimizing impedance match of rGO sponge metamaterials. Adv. Func. Mater. **32**(5), 2107508 (2022)
Wang, L., An, N., He, X., Zhang, X., Zhu, A., Yao, B., Zhang, Y.: Dynamic and active THz graphene metamaterial devices. Nanomaterials **12**(12), 2097 (2022)
Wu, Z., Kelp, G., Yogeesh, M.N., Li, W., McNicholas, K.M., Briggs, A., Rajeeva, B.B., Akinwande, D., Bank, S.R., Shvets, G., Zheng, Y.: Dual-band moiré metasurface patches for multifunctional biomedical applications. Nanoscale **8**(43), 18461–18468 (2016)
Xiao, S., Wang, T., Liu, T., Zhou, C., Jiang, X., Zhang, J.: Active metamaterials and metadevices: a review. J. Phys. D Appl. Phys. **53**(50), 503002 (2022)
Xie, W., Sun, P., Wang, J., Feng, H., Luo, Q., Xie, Q., Guo, L., Zhang, Z., Sun, J., Zhao, Q., Yun, M.: Polarization-independent dual narrow-band perfect metamaterial absorber for optical communication. Microw. Opt. Technol. Lett. **64**(7), 1310–1316 (2022)
Xiong, H., Ji, Q., Bashir, T., Yang, F.: Dual-controlled broadband terahertz absorber based on graphene and Dirac semimetal. Opt. Express **28**(9), 13884–13894 (2020)
Ye, Y.Q., Jin, Y., He, S.: Omnidirectional, polarization-insensitive and broadband thin absorber in the terahertz regime. JOSA B **27**(3), 498–504 (2010)
Yi, Y., Yi, Z., Zhao, F., Yang, H., Li, M., Wu, B., Gao, E., Yi, Y., Long, M.: Independently tunable triple-band infrared perfect absorber based on the square loops-shaped nano-silver structure. Physica E **139**, 115122 (2022)
Yu, P., Wu, J., Ashalley, E., Govorov, A., Wang, Z.: Dual-band absorber for multispectral plasmon-enhanced infrared photodetection. J. Phys. D Appl. Phys. **49**(36), 365101 (2016)
Zhang, B., Zhao, Y., Hao, Q., Kiraly, B., Khoo, I.C., Chen, S., Huang, T.J.: Polarization-independent dual-band infrared perfect absorber based on a metal-dielectric-metal elliptical nanodisk array. Opt. Express **19**(16), 15221–15228 (2011)
Zhang, H., Cheng, Y., Chen, F.: Quad-band plasmonic perfect absorber using all-metal nanostructure metasurface for refractive index sensing. Optik **229**, 166300 (2021)
Zhao, L., Liu, H., He, Z., Dong, S.: Design of multi-narrowband metamaterial perfect absorbers in near-infrared band based on resonators asymmetric method and modified resonators stacked method. Opt. Commun. **420**, 95–103 (2018a)
Zhao, L., Liu, H., He, Z., Dong, S.: All-metal frequency-selective absorber/emitter for laser stealth and infrared stealth. Appl. Opt. **57**(8), 1757–1764 (2018b)